

 OPEN ACCESS

International Journal of Structural Stability and Dynamics  
(2025) 2550049 (28 pages)  
© The Author(s)  
DOI: 10.1142/S021945542550049X



## Out-of-Plane Instability and Vibrations of a Flexible Circular Arch Under a Moving Load

Xingwei Zhao \*

*School of Energy and Power Engineering  
University of Shanghai for Science and Technology  
Shanghai 200093, P. R. China  
xingwzhao@usst.edu.cn*

G. H. M. van der Heijden \*

*Department of Civil, Environmental & Geomatic Engineering  
University College London, London WC1E 6BT, UK  
g.heijden@ucl.ac.uk*

Received 31 December 2023

Accepted 6 March 2024

Published 22 March 2024

Flexible lightweight arched structures are finding increasing use as components in smart engineering applications. Such structures are prone to various types of instability under moving transverse loads. Here, we study deformation and vibration of a hinged circular arch under a uniformly moving point load using geometrically-exact rod theory to allow for large pre- and post-buckling deformations. We first consider the quasi-statics problem, without inertia. We find that for arches with relatively large opening angle ( $\sim 160^\circ$ ) a sufficiently large traversing load will induce an out-of-plane flopping instability, instead of the in-plane collapse (snap-through) that dominates failure of arches with smaller opening angle. In a subsequent dynamics study, with full account of inertia, we then explore the effect of the speed of the load on this lateral buckling. We find speed to have a delaying (or even suppressing) effect on the onset of three-dimensional bending-torsional vibrations and instability. Based on numerical computations we propose a power law describing this effect. Our results highlight the role of inertia in the onset of elastic instability.

**Keywords:** Circular arch; out-of-plane buckling; large deformation; Cosserat rod; moving load; generalized- $\alpha$  method; delay effect.

### 1. Introduction

Vibrations of flexible and slender structures subjected to a traveling load, i.e. the moving force problem, have been extensively studied under the small-deformation

\*Corresponding authors.

This is an Open Access article published by World Scientific Publishing Company. It is distributed under the terms of the Creative Commons Attribution 4.0 (CC BY) License which permits use, distribution and reproduction in any medium, provided the original work is properly cited.

assumption, especially for straight beams in civil engineering applications.<sup>1–4</sup> Large deformation behavior of curved beams and arches has attracted increasing attention in recent years because of the development of lighter materials, novel design techniques and the interest in bioinspired structures, with wide applications in robotics, energy harvesting and other smart engineering systems.<sup>5–7</sup> Such flexible lightweight structures are prone to different types of instability under traveling loads.

It has long been recognized that a free-standing arch can fail by different modes of buckling.<sup>8–11</sup> Spoorenberg *et al.*<sup>12</sup> distinguish three types of buckling of a circular arch: in-plane anti-symmetric sideways buckling, in-plane symmetric snap-through buckling and out-of-plane buckling. Static analyses are performed numerically<sup>12</sup> and experimentally (for subtended angles between 90° and 180°).<sup>13</sup> In the first two types of buckling the arch undergoes planar deformations, with bending dominating the internal stress, while in out-of-plane buckling, flexural and torsional deformations are coupled in the arch response.

Arch buckling has been studied under various types of loading. In-plane elastic stability due to a point load at the midspan point of a circular arch was studied in Ref. 14. A planar dynamical analysis of a suddenly applied midspan point load was given in Ref. 15. In-plane snap-through of a shallow sinusoidal arch under a uniformly moving point load was studied in Ref. 16. Speed effects were considered and a safe speed zone without dynamic snap-through was identified. The present authors studied planar dynamics of a deep circular arch induced by a uniformly moving point load, including snap-through buckling, in Ref. 17.

Out-of-plane stability of a circular arch due to a uniformly distributed radial load was studied in Ref. 18, while out-of-plane buckling due to a uniformly distributed vertical load was studied in Ref. 19. Out-of-plane arch buckling due to a moving point load does not seem to have been studied so far, either quasi-statically or dynamically. Preliminary results on out-of-plane buckling of a beam prebuckled into an arch shape (i.e. no intrinsic arch) were reported in Ref. 20. In this paper, we consider both the quasi-statics and dynamics problem for a circular arch and in particular study the effect of the speed of the moving load on the onset of failure.

Arch instability has traditionally been taken as catastrophic structural failure that needs to be avoided as much as possible in civil engineering. More recently, however, buckling of curved beams has also inspired novel designs of functional materials and reconfigurable structures.<sup>5,6</sup> Through this development a good understanding of the post-buckling behavior is becoming more important. Full understanding of buckling and post-buckling behavior requires a three-dimensional (3D) formulation with a description of large in-plane as well as out-of-plane deformations. The Cosserat theory of thin rods<sup>21</sup> gives a geometrically-exact description suitable for situations in which large deformations may be expected. Here, we use the dynamics version of this theory to study arch deformations and vibrations due to a moving load. Previous statics studies have mainly concentrated on cases where the pre-buckling

displacements are small and can therefore be neglected.<sup>22,23</sup> In contrast, in order to deal with flexible structures, we compute the exact pre-buckling equilibrium and perform a proper linearization about this solution to find critical points of instability (bifurcations).

The paper is organized as follows. In Sec. 2, we introduce the 3D formulation of Cosserat rod dynamics. The numerical discretization is presented in Sec. 3. In Sec. 4, we perform a stability analysis by omitting all inertial terms in the equations and by using the magnitude of the (quasi-statically) moving load and its arclength position along the arch as bifurcation parameters. We identify the region in parameter space where out-of-plane instability occurs. A dynamical analysis of this out-of-plane buckling is then performed in Sec. 5 under gradual increase of the speed of the traveling load. We find that the moving load has a stabilizing effect in the sense that it delays the onset of buckling, the more so as the speed is increased, consistent with observations in Refs. 17 and 20. Conclusions follow in Sec. 6.

## 2. Three-Dimensional Cosserat Rod Formulation

We describe arch deformations by means of the geometrically-exact Cosserat theory of thin rods. The rod is taken to be inextensible and unshearable (a valid assumption for slender rods/arches whose length is much greater than its characteristic cross-sectional dimensions). For the background of Cosserat rod theory, see Ref. 21.

### 2.1. Kinematics

Let  $\mathbf{r}(s, t) : [0, L] \times \mathbb{R} \rightarrow \mathbb{R}^3$  be a smooth space curve of length  $L$  describing the centerline of the rod (see Fig. 1). Further, let  $\{\mathbf{d}_1(s, t), \mathbf{d}_2(s, t), \mathbf{d}_3(s, t)\}$  be a frame of orthonormal directors (the Cosserat triad) such that  $\mathbf{d}_1$  and  $\mathbf{d}_2$  span the cross-section of the rod, pointing along its principal bending axes, and  $\mathbf{d}_3 = \mathbf{d}_1 \times \mathbf{d}_2$  is perpendicular to it and tangent to the centerline. This body-centered frame describes the varying orientation of the rod's (rigid) cross-sections with respect to the fixed inertial frame  $\{\mathbf{e}_1, \mathbf{e}_2, \mathbf{e}_3\}$ .

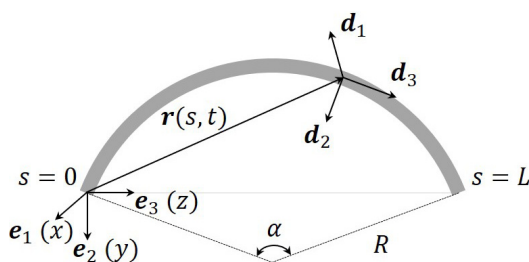


Fig. 1. Three-dimensional Cosserat rod model for a circular arch.

Orthonormality of the body frame implies the existence of two axial vectors,  $\kappa$  (the curvature vector) and  $\omega$  (the spin vector), such that

$$\partial_s \mathbf{d}_k = \kappa \times \mathbf{d}_k, \quad (2.1)$$

$$\partial_t \mathbf{d}_k = \omega \times \mathbf{d}_k, \quad (2.2)$$

where  $k = 1, 2, 3$  and  $\partial_s$  and  $\partial_t$  are partial derivatives with respect to the arch coordinate  $s$  and time  $t$ . These are the kinematic frame evolution equations.

## 2.2. Equations of motion

The balance laws for linear and angular momentum are given by

$$\partial_s \mathbf{n} + \mathbf{f} = \rho A \partial_{tt} \mathbf{r}, \quad (2.3)$$

$$\partial_s \mathbf{m} + \partial_s \mathbf{r} \times \mathbf{n} + \mathbf{l} = \rho \partial_t (\mathbf{I} \boldsymbol{\omega}), \quad (2.4)$$

where  $\mathbf{n}$  and  $\mathbf{m}$  are the resultant contact force and contact couple acting at the centerline at  $s$ , and  $\mathbf{f}$  and  $\mathbf{l}$  are external forces and moments acting on the rod.<sup>21</sup>  $\mathbf{I}$  is the moment of inertia tensor,  $A$  is the area of the cross-section and  $\rho$  is the density.

Since the rod is inextensible and unshearable, the director  $\mathbf{d}_3$  coincides with the tangent to the centerline of the rod, i.e.  $\partial_s \mathbf{r} = \mathbf{d}_3$ . If we also introduce the centerline velocity  $\mathbf{u} = \partial_t \mathbf{r}$ , then the identity  $\partial_t \partial_s \mathbf{r}(s, t) = \partial_s \partial_t \mathbf{r}(s, t)$  can be written as

$$\partial_t \mathbf{d}_3 = \partial_s \mathbf{u}. \quad (2.5)$$

Similarly, the identity  $\partial_t \partial_s \mathbf{d}_k(s, t) = \partial_s \partial_t \mathbf{d}_k(s, t)$ , on using (2.2), leads to the curvature-spin compatibility equation

$$\partial_s \boldsymbol{\omega} = \partial_t \kappa + \kappa \times \boldsymbol{\omega}. \quad (2.6)$$

When expressed in the body frame, Eqs. (2.3)–(2.6) are transformed into the following equations (using a bold roman font for triples of components in the body frame, for instance  $\mathbf{n} = (n_1, n_2, n_3)$ ,  $n_i = \mathbf{n} \cdot \mathbf{d}_i$ , writing  $\mathbf{k}$  and  $\mathbf{w}$  for the curvature and spin triples, respectively, and denoting  $\mathbf{I}$  on principal axes by  $\mathbf{I} = \text{diag}(I_1, I_2, J)$ ):

$$\begin{aligned} \rho A \partial_t \mathbf{u} &= \partial_s \mathbf{n} + \mathbf{k} \times \mathbf{n} - \rho A (\mathbf{w} \times \mathbf{u}) + \mathbf{f}, \\ \rho \mathbf{I} \partial_t \mathbf{w} &= \partial_s \mathbf{m} + \mathbf{k} \times \mathbf{m} + \mathbf{d}_3 \times \mathbf{n} - \rho (\mathbf{w} \times \mathbf{I} \mathbf{w}) + \mathbf{l}, \\ \partial_t \mathbf{k} &= \partial_s \mathbf{w} + \mathbf{k} \times \mathbf{w}, \\ \mathbf{0} &= \partial_s \mathbf{u} + \mathbf{k} \times \mathbf{u} - \mathbf{w} \times \mathbf{d}_3. \end{aligned} \quad (2.7)$$

(This transformation from inertial to body frame involves the replacements  $\partial_s \mathbf{u} = \partial_s \mathbf{u} + \mathbf{k} \times \mathbf{u}$ ,  $\partial_t \mathbf{u} = \partial_t \mathbf{u} + \mathbf{w} \times \mathbf{u}$  and similar for the other variables.)

We finally introduce linear constitutive relations between the curvature changes  $\mathbf{k} - \mathbf{k}^0$  and the (body) moments  $\mathbf{m}$ , taking the unstressed arch to be curved in the  $e_2 - e_3$  plane (see Fig. 1), so that its intrinsic curvature triple is given by  $\mathbf{k}^0 = (1/R, 0, 0)$ :

$$\mathbf{m} = \hat{\mathbf{K}}(\mathbf{k} - \mathbf{k}^0), \quad (2.8)$$

where  $\hat{\mathbf{K}} = \text{diag}(B_1, B_2, C)$ , with  $B_1 = EI_1$  and  $B_2 = EI_2$  the principal bending stiffnesses and  $C = GJ$  the torsional stiffness.  $E$  and  $G$  are Young's modulus and the shear modulus, respectively. The constitutive relation can be used to eliminate  $\mathbf{m}$  in (2.7) in favor of  $\mathbf{k}$ , thus giving us 12 equations for the body components  $(\mathbf{u}, \mathbf{w}, \mathbf{k}, \mathbf{n}) =: \mathbf{y}$  in the form

$$\mathbf{M}\partial_t\mathbf{y}(s, t) + \mathbf{K}\partial_s\mathbf{y}(s, t) + \mathbf{\Lambda}(s, t) = \mathbf{0}, \quad (2.9)$$

where  $\mathbf{M}$  and  $\mathbf{K}$  are mass and stiffness matrices (constant in the case of a uniform rod). Note that these matrices need to go inside the derivatives if they vary in time ( $\mathbf{M}$ ) or in space ( $\mathbf{K}$ ), but this is not the case here. All nonlinear terms in (2.7) are contained in the load vector  $\mathbf{\Lambda}$ . The same formulation is used in Ref. 24.

### 2.3. Computation of 3D rod shapes

Since we solve the rod formulations in the body frame instead of the fixed inertial frame, to compute rod shapes in space we need to postprocess the solution  $\mathbf{y}$  by subsequently either solving the equations in (2.1) and integrating the centerline equation  $\partial_s\mathbf{r} = \mathbf{d}_3$  or solving the equations in (2.2) and integrating the velocity  $\mathbf{u} = \partial_t\mathbf{r}$  to obtain  $\mathbf{r}$ . We define  $\mathbf{R}$  as the matrix whose columns are the frame vectors  $e_1, e_2, e_3$  represented in the body frame.  $\mathbf{R}$  is thus the rotation matrix from the inertial to the body frame, satisfying

$$\mathbf{e}_k = \mathbf{R}\mathbf{d}_k \quad (k = 1, 2, 3). \quad (2.10)$$

For any vector  $\mathbf{V}$  we have the following transformation rule for derivatives with respect to the different frames:

$$\partial_s\mathbf{V}|_{\{e_k\}} = \partial_s\mathbf{V}|_{\{d_k\}} + \mathbf{k} \times \mathbf{V}, \quad \partial_t\mathbf{V}|_{\{e_k\}} = \partial_t\mathbf{V}|_{\{d_k\}} + \mathbf{w} \times \mathbf{V} \quad (k = 1, 2, 3). \quad (2.11)$$

Applying these to the inertial frame vectors, we have

$$\partial_s\mathbf{e}_k = -\mathbf{k} \times \mathbf{e}_k = -\hat{\mathbf{k}}\mathbf{e}_k, \quad \partial_t\mathbf{e}_k = -\mathbf{w} \times \mathbf{e}_k = -\hat{\mathbf{w}}\mathbf{e}_k, \quad (2.12)$$

where  $\hat{\mathbf{k}}$  and  $\hat{\mathbf{w}}$  are the skew-symmetric matrices corresponding to  $\mathbf{k}$  and  $\mathbf{w}$ . It follows that

$$\partial_s\mathbf{R} = -\hat{\mathbf{k}}\mathbf{R}, \quad \partial_t\mathbf{R} = -\hat{\mathbf{w}}\mathbf{R}. \quad (2.13)$$

Assuming we choose to use the second equation in (2.13) (i.e. time integration), the rotation matrix is incrementally updated according to

$$\mathbf{R}(s, t + \Delta t) = e^{-\widehat{\Delta\theta}} \mathbf{R}(s, t), \quad (2.14)$$

with initial condition  $\mathbf{R}(0) = \mathbf{E}$  (the identity matrix) if the body frame at  $t = 0$  is aligned with the fixed frame.<sup>25</sup> Here,  $\widehat{\Delta\theta}$  is the skew-symmetric matrix of the incremental rotation vector  $\Delta\theta$  with respect to the spin vector  $\mathbf{w}$ , where

$$\Delta\theta = \frac{\mathbf{w}(s, t + \Delta t) + \mathbf{w}(s, t)}{2} \Delta t. \quad (2.15)$$

The exponential is conveniently computed by using the Rodrigues formula (valid for any skew-symmetric matrix  $\widehat{\mathbf{x}}$ )

$$e^{-\widehat{\mathbf{x}}} = \mathbf{E} - \widehat{\mathbf{n}} \sin |\mathbf{x}| + \widehat{\mathbf{n}}^2 (1 - \cos |\mathbf{x}|), \quad \mathbf{n} = \frac{\mathbf{x}}{|\mathbf{x}|}. \quad (2.16)$$

Having found  $\mathbf{R}$ , we finally obtain the centerline  $\mathbf{r}$  by integrating the velocity vector:

$$\partial_t \mathbf{r} = \mathbf{u} = \mathbf{R}^T \mathbf{u}. \quad (2.17)$$

Both the rotation matrix  $\mathbf{R}$  and the centerline  $\mathbf{r}$  can also be obtained by spatial integration subject to relevant boundary conditions.

#### 2.4. Quasi-static formulation

A quasi-static formulation is obtained by eliminating inertial terms in the rod dynamics equations. Omitting inertial terms in the equations of motion in (2.7), we have

$$\mathbf{n}' + \mathbf{k} \times \mathbf{n} + \mathbf{f} = \mathbf{0}, \quad (2.18)$$

$$\mathbf{m}' + \mathbf{k} \times \mathbf{m} + \mathbf{d}_3 \times \mathbf{n} + \mathbf{l} = \mathbf{0}, \quad (2.19)$$

where a prime,  $(\cdot)'$ , is used for derivatives with respect to  $s$ .

The kinematic frame evolution equation (2.1) gives

$$\mathbf{d}'_1 = \kappa_3 \mathbf{d}_2 - \kappa_2 \mathbf{d}_3, \quad (2.20)$$

$$\mathbf{d}'_2 = \kappa_1 \mathbf{d}_3 - \kappa_3 \mathbf{d}_1, \quad (2.21)$$

$$\mathbf{d}'_3 = \kappa_2 \mathbf{d}_1 - \kappa_1 \mathbf{d}_2. \quad (2.22)$$

Rod shapes can be computed by integrating the tangent director:

$$\mathbf{r}' = \mathbf{d}_3. \quad (2.23)$$

We again eliminate  $\mathbf{m}$  by using the linear constitutive law (2.8). We then have 18 equations for the variables  $(\mathbf{k}, \mathbf{n}, \mathbf{d}_1, \mathbf{d}_2, \mathbf{d}_3, \mathbf{r}) =: \mathbf{y}$  in the form

$$\mathbf{K}\mathbf{y}'(s) + \boldsymbol{\Lambda}(\mathbf{y}(s), s) = \mathbf{0}, \quad (2.24)$$

where  $\mathbf{K}$  is the (diagonal) stiffness matrix and  $\mathbf{\Lambda}$  is the load vector. We use this formulation for the bifurcation analysis. Solutions of these formulations are also taken as initial conditions for the dynamical problem.

### 2.5. Implementation of the traveling point load

The rotation matrix  $\mathbf{R}$  can be used to transform any external forces or moments specified in the fixed frame to the body frame for inclusion in (2.7):

$$\mathbf{f} = \mathbf{R}\mathbf{f}, \quad \mathbf{l} = \mathbf{R}\mathbf{l}. \quad (2.25)$$

We formulate the special case of a point load, required for our application, with the help of a Dirac- $\delta$  function:

$$\mathbf{f} = \delta(s - \sigma)F\mathbf{e}_2. \quad (2.26)$$

Here,  $\delta$  is the Dirac- $\delta$  function and  $\sigma$  is the instantaneous position where the moving point load, of magnitude  $F$ , is applied. Assuming that the load moves at a constant speed relative to the arch, we have  $\sigma = vt$ , where  $v$  is the speed of travel. Equation (2.25) is then used to transform the external load in the fixed frame to the body frame, for inclusion in either the dynamics formulation (2.9) or the statics formulation (2.24). We shall take  $\mathbf{l} = \mathbf{0}$ .

## 3. Numerical Method

### 3.1. Generalized- $\alpha$ method

The generalized- $\alpha$  method is a Newmark-like implicit integrator with desirable features such as second-order accuracy, unconditional stability and controllable numerical dissipation, first proposed by Chung and Hulbert<sup>26</sup> in 1993 for the numerical time integration of linear structural dynamics equations. Erlicher *et al.*<sup>27</sup> verified the accuracy and stability of the method when applied to nonlinear dynamics problems. We apply the generalized- $\alpha$  method to the dynamics formulation in (2.9) for both spatial and temporal discretization, as in Refs. 17 and 24.

In the first step, we derive the semi-discrete form of (2.9) with respect to time as

$$(\mathbf{M}\partial_t\mathbf{y})^{1-\alpha_t} + (\mathbf{K}\partial_s\mathbf{y})^{1-\beta_t} + \mathbf{\Lambda}^{1-\beta_t}(\mathbf{y}) = \mathbf{0}, \quad (3.1)$$

where  $(\cdot)^{1-\iota} = (1-\iota)(\cdot)^i + \iota(\cdot)^{i-1}$ .  $\alpha_t$  and  $\beta_t$  average in time the inertial term and terms of the stiffness matrix and load vector, respectively.  $\mathbf{M}$  and  $\mathbf{K}$  are constant in our case. As to the treatment of the nonlinear  $\mathbf{\Lambda}^i$  term, we choose the generalized trapezoidal rule (one of the three quadrature rules summarized in Ref. 27), which

corresponds to setting  $\boldsymbol{\Lambda}^i(\mathbf{y}) = \boldsymbol{\Lambda}(\mathbf{y}^i)$ . Then  $\boldsymbol{\Lambda}^{1-\beta_t}(\mathbf{y}) = (1 - \beta_t)\boldsymbol{\Lambda}(\mathbf{y}^i) + \beta_t\boldsymbol{\Lambda}(\mathbf{y}^{i-1})$  and (3.1) becomes

$$\begin{aligned} & \mathbf{M}[(1 - \alpha_t)\partial_t \mathbf{y}^i + \alpha_t \partial_t \mathbf{y}^{i-1}] \\ & + \mathbf{K}[(1 - \beta_t)\partial_s \mathbf{y}^i + \beta_t \partial_s \mathbf{y}^{i-1}] + (1 - \beta_t)\boldsymbol{\Lambda}(\mathbf{y}^i) + \beta_t\boldsymbol{\Lambda}(\mathbf{y}^{i-1}) = \mathbf{0}. \end{aligned} \quad (3.2)$$

Similarly, applying the generalized- $\alpha$  method in space gives

$$\begin{aligned} & \mathbf{M}\{(1 - \alpha_t)[(1 - \alpha_s)\partial_t \mathbf{y}_j^i + \alpha_s \partial_t \mathbf{y}_{j-1}^i] + \alpha_t[(1 - \alpha_s)\partial_t \mathbf{y}_j^{i-1} + \alpha_s \partial_t \mathbf{y}_{j-1}^{i-1}]\} \\ & + \mathbf{K}\{(1 - \beta_t)[(1 - \beta_s)\partial_s \mathbf{y}_j^i + \beta_s \partial_s \mathbf{y}_{j-1}^i] + \beta_t[(1 - \beta_s)\partial_s \mathbf{y}_j^{i-1} + \beta_s \partial_s \mathbf{y}_{j-1}^{i-1}]\} \\ & + \{(1 - \beta_t)[(1 - \beta_s)\boldsymbol{\Lambda}_j^i + \beta_s\boldsymbol{\Lambda}_{j-1}^i] + \beta_t[(1 - \beta_s)\boldsymbol{\Lambda}_j^{i-1} + \beta_s\boldsymbol{\Lambda}_{j-1}^{i-1}]\} = \mathbf{0}. \end{aligned} \quad (3.3)$$

In this equation, the superscript indicates the time step while the subscript indicates the spatial step, i.e. the node of the discretized curve.

In the second step, the  $s$  and  $t$  derivatives are approximated as

$$\partial_t \mathbf{y}^i = \frac{\mathbf{y}^i - \mathbf{y}^{i-1}}{\gamma_t \Delta t} - \frac{1 - \gamma_t}{\gamma_t} \partial_t \mathbf{y}^{i-1}, \quad \partial_s \mathbf{y}_j = \frac{\mathbf{y}_j - \mathbf{y}_{j-1}}{\gamma_s \Delta s} - \frac{1 - \gamma_s}{\gamma_s} \partial_s \mathbf{y}_{j-1}, \quad (3.4)$$

where  $\Delta s$  and  $\Delta t$  are the spatial step size and time step size, respectively. By substituting (3.4) into (3.3), we obtain a system of algebraic equations in the form

$$\mathbf{F}_j^i := \mathbf{A}(\mathbf{y}_j^i) + \mathbf{B}(\mathbf{y}_{j-1}^i) - \zeta \partial_s (\mathbf{K} \mathbf{y})_{j-1}^i - \boldsymbol{\Gamma}_{j-1}^{i-1} = \mathbf{0} \quad (3.5)$$

with

$$\zeta = \frac{(1 - \beta_t)(1 - \beta_s - \gamma_s)}{\gamma_s}.$$

Here,  $\mathbf{A}(\mathbf{y}_j^i)$  and  $\mathbf{B}(\mathbf{y}_{j-1}^i)$  are nonlinear functions of the unknown variables, while  $\boldsymbol{\Gamma}_{j-1}^{i-1} := \boldsymbol{\Gamma}_{j-1}^{i-1}(\mathbf{y}_j^{i-1}, \mathbf{y}_{j-1}^{i-1}, \partial_t \mathbf{y}_j^{i-1}, \partial_t \mathbf{y}_{j-1}^{i-1}, \partial_s \mathbf{y}_j^{i-1}, \partial_s \mathbf{y}_{j-1}^{i-1})$  is known once variables at the earlier time step  $\mathbf{y}^{i-1}$  are solved. Each set of three parameters  $\alpha_s$ ,  $\beta_s$ ,  $\gamma_s$  and  $\alpha_t$ ,  $\beta_t$ ,  $\gamma_t$  can be expressed as functions of  $\lambda^\infty$ , the eigenvalue of the amplification matrix at infinity<sup>26</sup>:

$$\alpha(\cdot) = \frac{3\lambda_{(\cdot)}^\infty + 1}{2\lambda_{(\cdot)}^\infty - 2}, \quad \beta(\cdot) = \frac{\lambda_{(\cdot)}^\infty}{\lambda_{(\cdot)}^\infty - 1}, \quad \gamma(\cdot) = \frac{1}{1 - \lambda_{(\cdot)}^\infty}, \quad (3.6)$$

where  $\lambda_{(\cdot)}^\infty \in [-1, 0]$ . Note that  $\beta(\cdot) + \gamma(\cdot) = 1$  and hence

$$\zeta = 0.$$

This allows us to eliminate the terms with  $\zeta$  in (3.5), thereby significantly simplifying the Jacobian matrix  $\partial \mathbf{F}_j^i / \partial \mathbf{y}_k^i$  of the nonlinear system of equations without loss of either accuracy or numerical stability. We choose  $\lambda_s^\infty = \lambda_t^\infty = -1$ , corresponding to a value of 1/2 for all six parameters, which gives a stable second-order scheme without numerical damping.

The final system of algebraic equations (3.5) is solved using the global Newton code NLEQ1<sup>28</sup> with Jacobian matrix  $\partial \mathbf{F}_j^i / \partial \mathbf{y}_k^i$  provided analytically.

### 3.2. Numerical strategy for the implementation of a traveling load

The numerical implementation of the point load  $F$  represented by a Dirac- $\delta$  function needs special care. This representation is really an idealization of the real situation in which the force is applied over a small but finite interval, taken to the continuum point limit. In our discrete numerical treatment it makes sense to step back and replace the point load by a distributed load acting at grid points near the point load and statically equivalent with this point load. Thus, we apply Eftekhar's<sup>29</sup> approach and distribute the moving point force over spatially neighboring intervals  $[j - 2^{k-1}, j + 2^{k-1}]$ , with the center  $s_j = \sigma$  at the position of the original point load (see Fig. 2).

The simplest choice is to distribute a point force  $F$  over two neighboring intervals  $[s_{j-1}, s_{j+1}]$  by setting  $k = 1$ . The point load (2.26) then takes the discretized form

$$\mathbf{f}_j = \frac{F}{\Delta s} \mathbf{e}_2, \quad \mathbf{f}_{j+1} = \mathbf{f}_{j-1} = \mathbf{0}. \quad (3.7)$$

With this strategy the integral of the distributed load is equivalent to the magnitude of the original point force in the sense of force balance and the moment is balanced at the point where the moving load is located. This requires the existence of a discrete node wherever the moving point load is located, which may not always be possible or desirable in all situations, but is suitable and effective for our traveling load problem: since the speed  $v$  of the moving load is constant we can take  $\Delta t = \Delta s/v$  in our spatio-temporal discretization, thereby ensuring that the solution is sampled at times when the load is applied exactly at a node. This avoids the need for (error-introducing) interpolation of the point load and is convenient for code implementation.

## 4. Quasi-Static Stability Analysis

Here, we carry out a quasi-static analysis. This provides the “background” stability picture for the dynamical analysis in the following section. We are interested in the

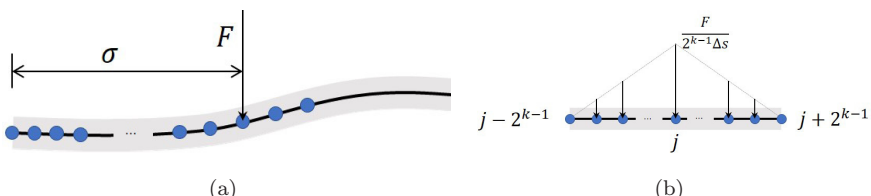


Fig. 2. (a) Point load acting on a discretized arch. (b) Numerical distribution of the point load over the  $[j - 2^{k-1}, j + 2^{k-1}]$  interval.

effect the speed of the traveling load has on arch stability, in particular the delay effect of this speed on out-of-plane instability. We will quantify this delay effect by extrapolating the onset of instability back to the case of zero speed, so it is good to consider this (quasi-)static case first. Knowing the equilibrium solutions of the system will also help us interpret dynamical oscillations later.

Static in-plane stability under varying midspan point load  $F$  has been studied in the literature before.<sup>14</sup> Planar stability under both varying magnitude and varying position of the point load has also been considered within an approximate, shallow-arch, context.<sup>16</sup> We here perform a geometrically-exact 3D quasi-static stability analysis in which both the magnitude  $F$  of the load and its arclength position  $\sigma$  are varied. For this analysis we solve Eq. (2.24) subject to hinged boundary conditions using the well-tested software AUTO,<sup>30</sup> which uses parameter continuation and allows the user to switch solution branches at branching points (bifurcations, instabilities).

The configuration of the arch is shown in Fig. 1. The ends of the arch are fixed in position and allowed to hinge freely about out-of-plane axes parallel to  $e_1$ . We set the length to be  $L = 1$  m. The height-span ratio of the arch is then characterized by either the opening angle  $\alpha$  or the radius of curvature  $R = L/\alpha$ . The cross-section of the arch is taken circular with radius  $r = 0.005$  m, giving  $I_1 = I_2 = I = \frac{\pi}{4}r^4$ . We furthermore take for the physical parameters: density  $\rho = 1\,500\,\text{kg/m}^3$ , Young's modulus  $E = 2.5\,\text{GPa}$  and Poisson's ratio  $\nu = 0.25$ . The shear modulus is  $G = E/[2(1 + \nu)]$ . Gravity of the arch is ignored because its magnitude is small compared to typical point loads required to buckle the arch: with the above parameter values the dimensionless weight parameter is  $\rho g A L^3/(EI) = 0.9408$ , while the dimensionless value of a typical instability-causing point load (see below) is 36.

Our numerical calculations reveal that to have an out-of-plane instability the arch needs to have a relatively large opening angle ( $\alpha \gtrsim 160^\circ$ ). Instability of arches with smaller opening angle is dominated by in-plane collapse (snap-through) with no stable path spanning the entire arch from  $\sigma = 0$  to  $\sigma = L$ . Figure 3 shows the stability diagram for  $\alpha = 160^\circ$  with curves of pitchfork bifurcations (BPs) and folds or limit points (LPs) delineating parameter regions of different types of arch instability. No instability is encountered for dimensionless loads  $FL^2/EI$  smaller than about 34.

Bifurcation diagrams, i.e. cuts through this stability diagram, at fixed values of  $FL^2/EI$  are given in Figs. 4–7 and illustrate arch instability at larger values of  $F$ .  $x$ ,  $y$  and  $z$  in these figures denote the components of  $\mathbf{r}$  relative to the fixed frame  $\{e_1, e_2, e_3\}$ . Solid branches carry stable, dashed branches unstable solutions. Fig. 4, for  $FL^2/EI = 50$  (triangles in Fig. 3), shows that for relatively large  $F$  (to the right of the filled circle at  $FL^2/EI = 47.5670$  in Fig. 3) the bifurcation diagram has a fold or LP (triangle in Fig. 4(a)) preventing passage of the load (starting at  $\sigma = 0$ ) beyond this limit. However, already before this limit is reached, stability of the main

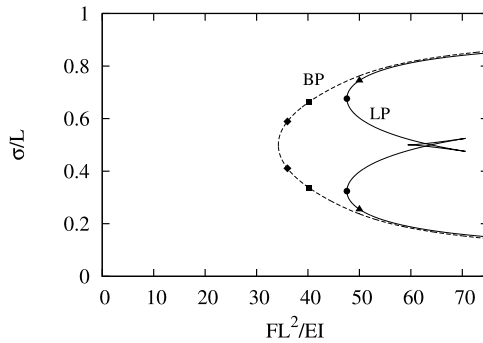


Fig. 3.  $F-\sigma$  parameter plane with curves of BPs and LPs delineating parameter regions of different types of arch instability. Markers at  $FL^2/EI = 36$  (diamonds), 40.1657 (squares), 47.5670 (circles) and 50 (triangles) are discussed in the text. ( $\alpha = 160^\circ$ .)

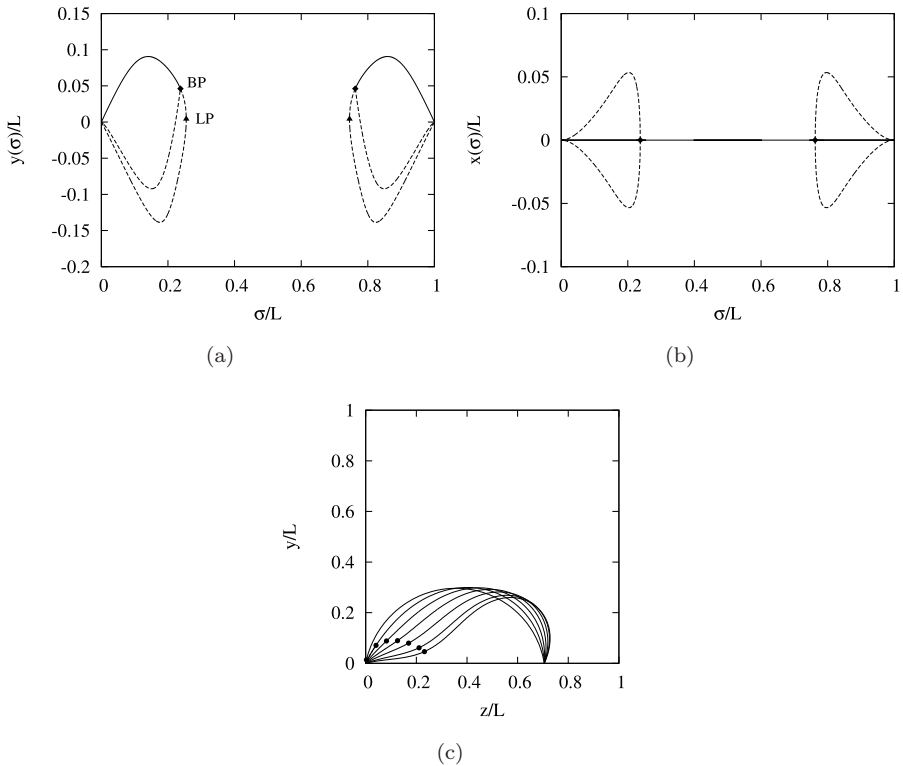


Fig. 4. (a) and (b) Bifurcation diagrams for  $FL^2/EI = 50$  showing a LP (triangle) along the main branch as well as a bifurcating branch of 3D solutions (with either  $x > 0$  or  $x < 0$ ) coming out of a (subcritical) BP (diamond). Solid branches are stable, dashed branches unstable. The arch suffers in-plane snap-through at the BP. (c) True view arch shapes at various points along the stable branch in (a). Dots mark the position of the load. The last shape corresponds to the critical point of snap instability (pitchfork). ( $\alpha = 160^\circ$ .)

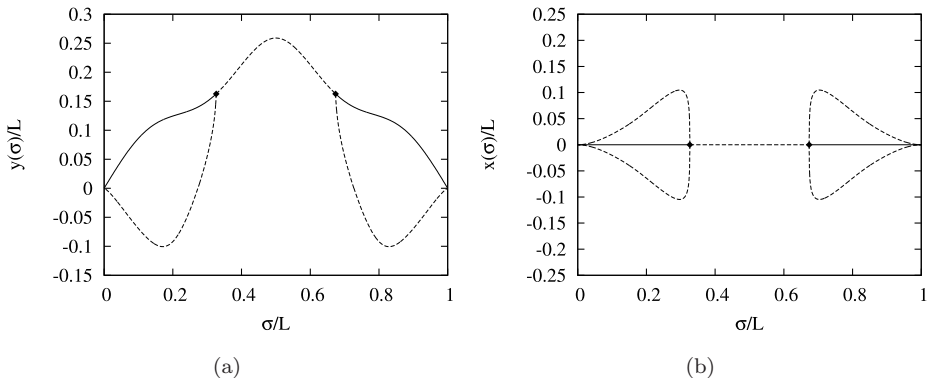


Fig. 5. Bifurcation diagrams for  $FL^2/EI = 41$  showing a main branch spanning from  $\sigma = 0$  to  $\sigma = L$  with subcritical BPs (diamonds). (a) Vertical in-plane displacement  $y(\sigma)$  at the position  $\sigma$  of the load. (b) Out-of-plane displacement  $x(\sigma)$ . ( $\alpha = 160^\circ$ .)

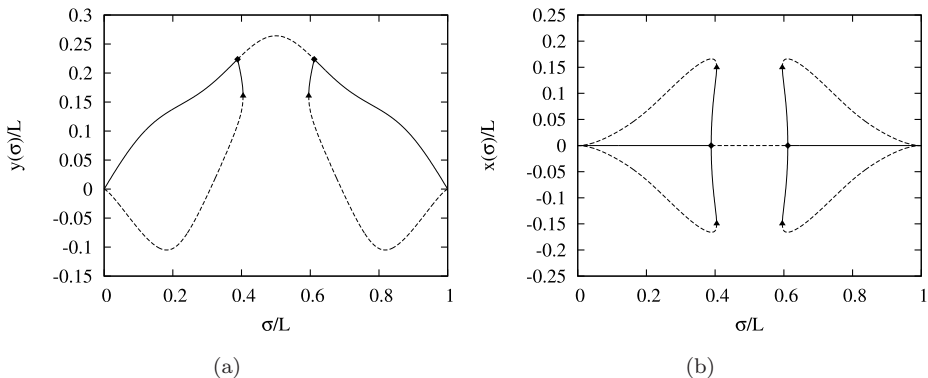


Fig. 6. Bifurcation diagrams for  $FL^2/EI = 37$  showing a main branch spanning from  $\sigma = 0$  to  $\sigma = L$  with supercritical BPs (diamonds). (a) Vertical in-plane displacement  $y(\sigma)$  at the position  $\sigma$  of the load. (b) Out-of-plane displacement  $x(\sigma)$ . ( $\alpha = 160^\circ$ .)

solution branch is lost in a BP (diamond in Fig. 4(a)). Out of this bifurcation comes a branch of 3D solutions (with out-of-plane displacement  $x$  shown in Fig. 4(b)), but because the branch is subcritical these solutions are unstable. The arch will therefore suffer in-plane snap buckling when the diamond is reached. By symmetry, a similar set of solution branches exists near  $\sigma/L = 1$ , relevant when the load enters the arch from its right end. Figure 4(c) shows arch shapes before the collapse, with positions of the load (entering from the left) indicated. Clearly, the arch experiences significant pre-buckling deformation.

At the lower value of  $FL^2/EI = 41$  (Fig. 5) there are no LPs any more: solution branches have merged and the main branch spans across from  $\sigma = 0$  to  $\sigma = L$ . Arch failure, however, is still in a subcritical BP, causing in-plane collapse.

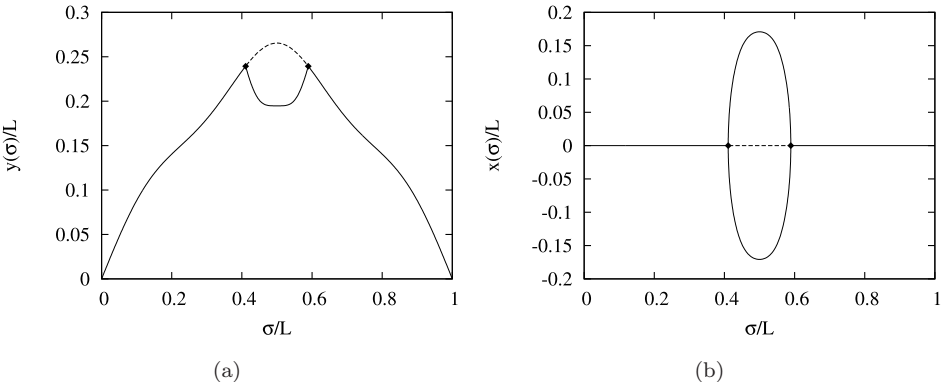


Fig. 7. Bifurcation diagrams for  $FL^2/EI = 36$  showing the vertical in-plane displacement  $y(\sigma)$  (a) and the out-of-plane displacement  $x(\sigma)$  (b) of the arch at the position  $\sigma$  of the load. ( $\alpha = 160^\circ$ .)

At  $FL^2/EI = 37$  (Fig. 6) the BP has become supercritical, which has created a stable branch of 3D out-of-plane solutions. However, this 3D branch has a fold (triangle in Fig. 6(a)), where the arch again suddenly collapses, but now from a 3D configuration. The critical value of transition from sub- to supercritical behavior occurs at  $FL^2/EI = 40.1657$  (squares in Fig. 3).

Finally, at  $FL^2/EI = 36$  (Fig. 7) the bifurcating 3D branches from the left and right halves of the arch have merged as well and a stable branch of 3D solutions spans across the midpoint of the arch. This merger occurs at  $FL^2/EI = 36.4915$ . At  $\sigma/L = 0.410740$  a supercritical BP occurs (diamond in Fig. 3), generating a branch of stable out-of-plane solutions (with either  $x > 0$  or  $x < 0$ , see Fig. 7(b)). Upon further increase of  $\sigma$  a reverse BP occurs at (the symmetrically related point)  $\sigma/L = 0.589260$ , where the main branch of planar arch solutions is restabilized. The maximum lateral displacement is  $x_{\max}/L = 0.170815$ , reached at  $\sigma/L = 0.5$ .

Thus, for the narrow window of loads between  $FL^2/EI = 34.2342$  (the lowest  $F$  along the BP curve in Fig. 3) and  $FL^2/EI = 36.4915$  the arch gently flops sideways but then recovers a 2D shape when the load reaches the symmetrically related position on the other side of the arch. For loads between  $FL^2/EI = 36.4915$  and  $FL^2/EI = 40.1657$  the arch suddenly fails in 3D. And for loads larger than  $FL^2/EI = 40.1657$  the arch suddenly fails in 2D. In the following section, we will explore whether, and to what extent, the statically stable out-of-plane solutions are observed in true inertial dynamics.

We end this quasi-static analysis by commenting that we do not find the in-plane symmetry-breaking sideways buckling mode listed in Ref. 12 because our arch is always loaded asymmetrically (the load enters from the left end of the arch).

## 5. Dynamical Analysis

Following the stability analysis in Sec. 4, we can predict that an arch with an opening angle of  $\alpha = 160^\circ$  fails by out-of-plane flopping under the action of a point force in the vertical ( $e_2$ ) direction with a magnitude of  $FL^2/EI = 36$ , once this force enters the interval  $\sigma/L \in [0.410740, 0.589260]$  (from either side). For the real dynamical problem the arch never regains stability once it fails sideways (except perhaps eventually under damping).

### 5.1. Initial solution

To avoid numerical distraction of instantaneous waves due to the sudden application of a point force at the boundary  $t = 0$ , one can either set some numerical damping to damp out high-frequency waves, or take the effects of the point force into account as initial solution, starting the dynamical analysis at  $t = 0^+$ . In this paper, we take the latter approach and prepare an initial solution with stress discontinuity at the arch boundary using the quasi-static Eq. (2.24) with hinged boundary conditions at both ends,

$$\begin{aligned} s = 0 : \quad \kappa_1 &= 1/R, \quad y = 0, \quad z = 0, \\ s = L : \quad \kappa_1 &= 1/R, \quad y = 0, \quad z = 2R \sin \alpha/2. \end{aligned} \tag{5.1}$$

The configuration of the arch in this initial state is shown in Fig. 8(a). The discontinuity of the internal force  $\mathbf{n}$  due to a point force  $FL^2/EI = 36$  acting at the pinned end  $s = 0$  in this initial state is displayed in Fig. 8(b). We prepare this solution as starting solution at  $t = 0^+$  for the subsequent transient dynamical analysis.

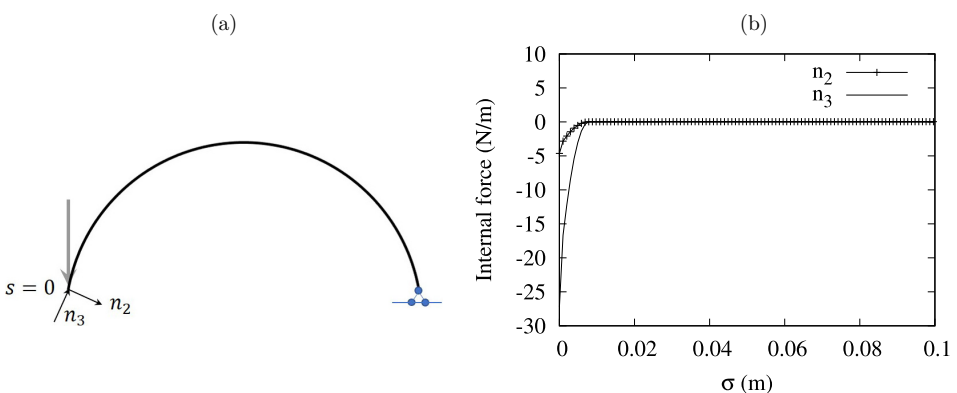


Fig. 8. (a) Initial configuration of the hinged arch with point load at  $s = 0$ . (b) In-plane shear force  $n_2$  and tension  $n_3$  in the arch induced by a point load  $FL^2/EI = 36$  at  $s = 0$ .

## 5.2. Dynamical solutions

We study the transient dynamical problem for the arch under a moving load at different speeds. The moving load is assumed to be always applied in the vertical ( $e_2$ ) direction while it travels along the arch. A trivial force with a magnitude of  $O(10^{-10})$  is introduced in the (initially out-of-plane) direction  $d_1$  along the arch as a perturbation to induce out-of-plane deformation once the planar solution has gone unstable. Without this artificial perturbation we would only compute unstable planar solutions for a perfectly planar arch under perfectly planar loading.

For this dynamical problem the hinged-hinged boundary conditions with fixed (i.e. non-moving) ends can be formulated as

$$\begin{aligned} s = 0, L : \quad & \mathbf{u} = u_1 d_1 + u_2 d_2 + u_3 d_3 = \mathbf{0}, \\ & \mathbf{k} \cdot \mathbf{e}_1 = \kappa_1 d_{11} + \kappa_2 d_{21} + \kappa_3 d_{31} = 0, \\ & \mathbf{w} \cdot \mathbf{e}_2 = \omega_1 d_{12} + \omega_2 d_{22} + \omega_3 d_{32} = 0, \\ & \mathbf{w} \cdot \mathbf{e}_3 = \omega_1 d_{13} + \omega_2 d_{23} + \omega_3 d_{33} = 0. \end{aligned} \tag{5.2}$$

For reference we derive the natural frequencies of small in-plane and out-of-plane vibrations in Appendices A and B, respectively. As a convenient measure for the speed of the moving load we define  $\eta$  to be the fraction of  $v$  of the speed required to cross the arch in a period of its fundamental in-plane bending mode, i.e.

$$v = \eta v_1, \quad \text{where } v_1 = \omega_1^{\text{in}} L / (2\pi) = 12.8950 \text{ m/s},$$

where  $\omega_1^{\text{in}}$  is given in (A.3). (We recall that the first classical resonance speed is  $v_{\text{cri}} = \omega_1^{\text{in}} L / \pi^{1.4}$ )

For the arch we consider in this paper, the period of the first in-plane bending mode is  $T_1^{\text{in}} = 2\pi/\omega_1^{\text{in}} = 0.0775496 \text{ s}$ , while the period of the first out-of-plane bending-torsional mode is  $T_1^{\text{out}} = 2\pi/\omega_1^{\text{out}} = 0.102199 \text{ s}$ , where  $\omega_1^{\text{out}}$  is given in (B.3). The maximum number of periods of in-plane and out-of-plane vibrations an arch can undergo when the point load travels along the arch at a speed of  $v$  are, respectively,  $N_{\max}^{\text{in}} = \frac{L}{vT_1^{\text{in}}}$  and  $N_{\max}^{\text{out}} = \frac{L}{vT_1^{\text{out}}}$ . To observe periodic out-of-plane oscillations of the arch, we need to maintain  $N_{\max}^{\text{out}} = \frac{L}{vT_1^{\text{out}}} = \frac{L}{\eta v_1 T_1^{\text{out}}} = \frac{1}{2\eta} \frac{T_1^{\text{in}}}{T_1^{\text{out}}}$  as a sufficiently large number.

Considering that the arch buckles by out-of-plane flopping for  $\sigma \in [0.410740, 0.58926]$  in the quasi-static analysis (see Fig. 7(b)), we require

$$\frac{L - \sigma_0}{L} N_{\max}^{\text{out}} = \frac{L - \sigma_0}{L} \frac{1}{2\eta} \frac{T_1^{\text{in}}}{T_1^{\text{out}}} > N_{\exp},$$

where  $\sigma_0/L = 0.410740$  is the position of the load at the onset of out-of-plane buckling and  $N_{\exp}$  is the number of out-of-plane periods we expect to see during

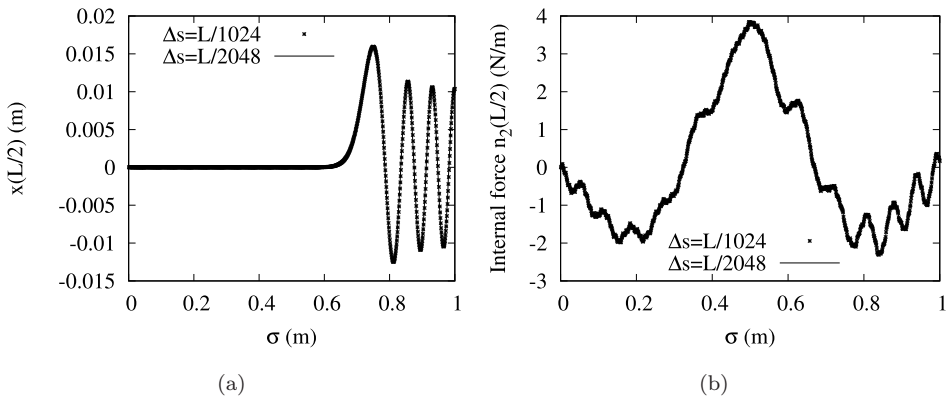


Fig. 9. Convergence test for a case of out-of-plane instability at a traveling speed of  $\eta = 0.05$ : (a) lateral midspan position  $x(L/2)$ , (b) in-plane midspan shear force  $n_2(L/2)$ .

the full time span of a point load traveling along the arch. By setting  $N_{\text{exp}} = 1$  we find the maximum reference speed

$$\eta < \frac{L - \sigma_0}{2LN_{\text{exp}}} \frac{T_1^{\text{in}}}{T_1^{\text{out}}} =: \eta_{\max} \quad \text{and} \quad \eta_{\max} = 0.223567.$$

Since the load travels along the arch within a finite time interval, for speeds larger than  $\eta_{\max}v$ , the load does not stay on the arch long enough to excite a single period of out-of-plane vibrations. We shall therefore study the effects of moving speeds on transient vibrations and out-of-plane buckling of arches for  $\eta < \eta_{\max}$ . We find that when the load is moving at  $\eta = 0.16$  (Fig. 10(a)) the lateral displacement of the midspan when the load travels along the arch is at a scale of  $O(10^{-8})$ , which is of the same magnitude as the numerical precision we set in the numerical code. We therefore declare that the arch is not buckled for the case of  $\eta = 0.16$ . Recall that  $\sigma$ , i.e. the instantaneous position of the moving load, displayed along the horizontal axes in the figure, is a time-like variable since  $\sigma = vt$ .

To help us choose suitable step sizes for our numerical runs we perform a convergence test. Maintaining accuracy may be particularly challenging at sudden (in-plane or out-of-plane) instabilities. Results of the test are presented in Fig. 9. The figure shows the lateral midspan position  $x(L/2)$  and in-plane midspan shear force  $n_2(L/2)$  for  $\eta = 0.05$  and different spatial step sizes. It is seen that step sizes  $\Delta s = L/1024$  and  $\Delta s = L/2048$  do not lead to noticeable differences. Thus, we deem the numerical method to have converged and we take  $\Delta s = L/2048$  and simultaneously  $\Delta t = \Delta s/\eta v_1$  in all the other runs in this section.

Figure 10 shows that for gradually decreasing speed  $\eta$ , we find a maximum lateral displacement of the arch midspan of  $O(10^{-7})$ ,  $O(10^{-6})$ ,  $O(10^{-4})$ ,  $O(10^{-2})$  for  $\eta = 0.1$ ,  $\eta = 0.08$ ,  $\eta = 0.06$  and  $\eta = 0.05$ , respectively. These lateral displacements

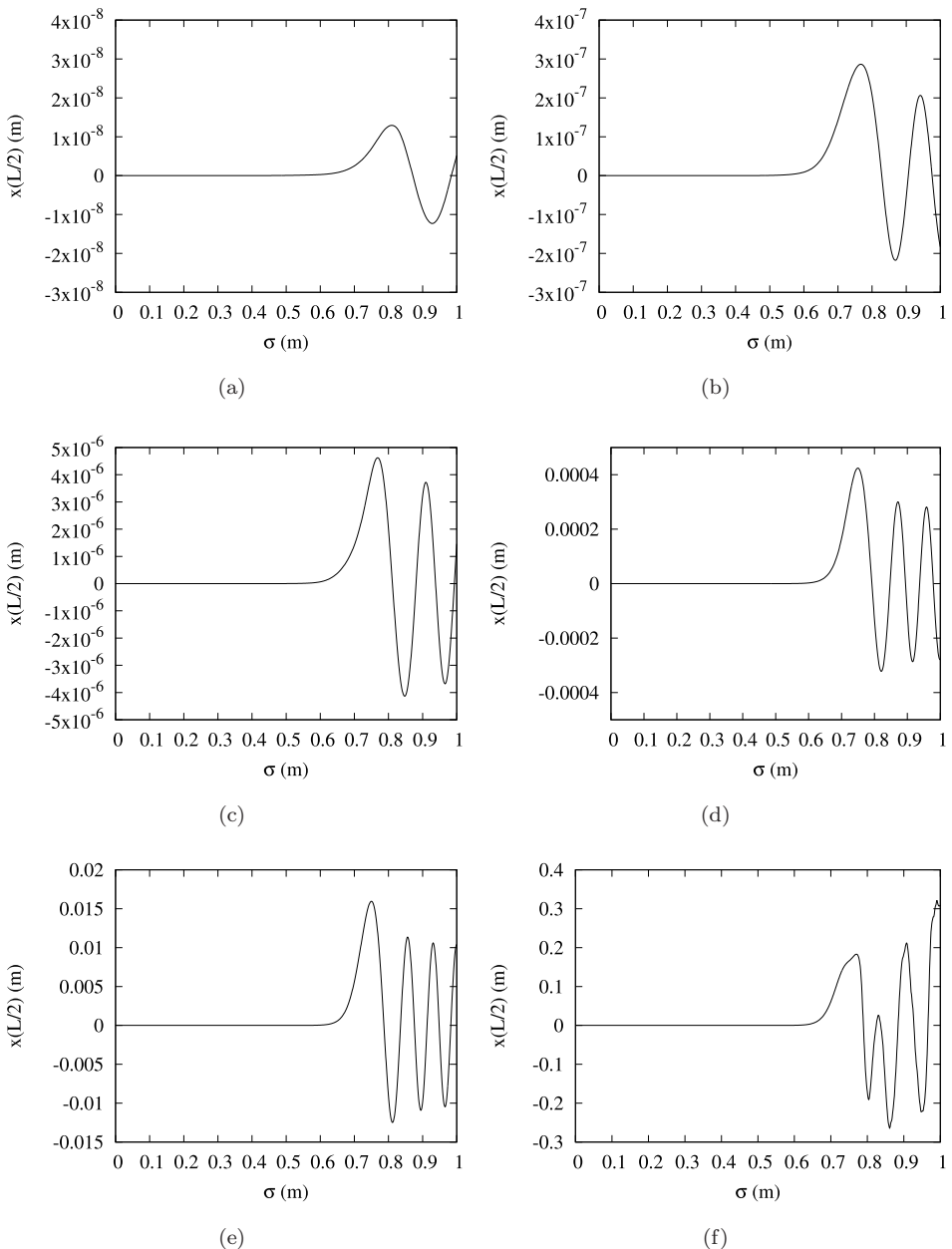


Fig. 10. Lateral midspan position of the arch at decreasing traveling speeds: (a)  $\eta = 0.16$ , (b)  $\eta = 0.1$ , (c)  $\eta = 0.08$ , (d)  $\eta = 0.06$ , (e)  $\eta = 0.05$  and (f)  $\eta = 0.045$ .

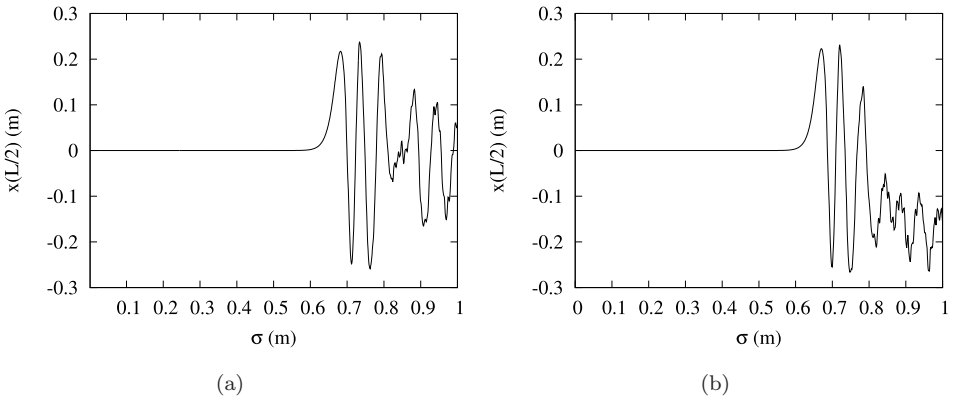


Fig. 11. Lateral midspan position of the arch at (a)  $\eta = 0.04$  and (b)  $\eta = 0.039$ .

are all of smaller magnitude than the quasi-static out-of-plane displacement predicted in Fig. 7(b), and decrease as the speed goes up. We conclude, therefore, that the out-of-plane buckling mode of an arch is softened or even suppressed due to the relatively high speed of the traveling point load when  $\eta > 0.05$ . The higher the traveling speed, the smaller the out-of-plane buckling displacement.

For the speed  $\eta = 0.045$  (Fig. 10(f)) the midspan displacement eventually becomes of the order of the quasi-static out-of-plane displacement seen in Fig. 7(b), after a significant delay. Results for even lower speeds are given in Fig. 11. In Fig. 11(a), for  $\eta = 0.04$ , the vibrations take place about the statically unstable planar equilibrium solution having  $x = 0$  (dashed line in Fig. 7(b)). In Fig. 11(b), for  $\eta = 0.039$ , vibrations take place about the statically stable out-of-plane solution, with  $x < 0$ , in Fig. 7(b). The  $x < 0$  branch is consistent with the direction of the artificial perturbation applied in our numerical calculations.

We define  $\sigma_{\text{cri}}$  to be the instantaneous arclength position of the point load along the arch when buckling is induced. The dimensionless instantaneous positions of the point load at buckling are approximately  $\sigma_{\text{cri}}/L = 0.62$  and  $\sigma_{\text{cri}}/L = 0.61$ , for  $\eta = 0.04$  and  $\eta = 0.039$ , respectively, i.e. significantly higher than the critical  $\sigma_{\text{cri}}$  predicted in Fig. 7(b). There is therefore a delay effect on buckling due to the speed of the traveling load. This is consistent with our earlier findings in Refs. 17 and 20. The phenomenon is similar to the delay of instability found in our previous numerical work<sup>31</sup> on the torsional buckling of rods under a dynamically applied load at varying angular velocities, and in analytical work in Ref. 32 on elastic snap-through due to a dynamically varying control parameter. Complex flexural-torsional coupling effects are excited when the arch flops out-of-plane as shown by the dramatic oscillations of internal stress at the midspan of the arch seen in Fig. 12.

Data on the onset of the out-of-plane instability are summarized in Table 1, where a few smaller speeds are listed as well. Results for even smaller speeds become

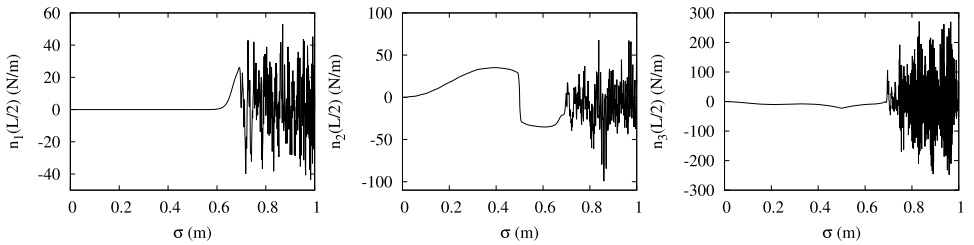


Fig. 12. Internal stress components of the arch midspan in the body frame ( $\eta = 0.04$ ).

Table 1. Lateral midspan position  $x_{\max}$  and critical buckling position  $\sigma_{\text{cri}}$  at various load speeds  $\eta$ .

Speed $\eta$	$x_{\max}/L$	Critical buckling position $\sigma_{\text{cri}}/L$
0 (quasi-static)	$\bar{x} = 0.170815$	0.410740
0.025	$>\bar{x}$	0.501936
0.03	$>\bar{x}$	0.540491
0.035	$>\bar{x}$	0.577978
0.039	$>\bar{x}$	0.612394
0.04	$>\bar{x}$	0.621759
0.045	$>\bar{x}$	0.661603
0.05	0.015	suppressed
0.06	$O(10^{-4})$	suppressed
0.08	$O(10^{-6})$	suppressed
0.1	$O(10^{-7})$	suppressed
0.16	$O(10^{-8})$	stable

prohibitively expensive computationally because our numerical method relies on the point load being at a node at each time step ( $\Delta s = v\Delta t$ ). We see that due to real dynamical effects the maximum lateral deflection of the midspan is of the same order of magnitude as predicted in Fig. 7(b), but can exceed it when out-of-plane buckling is fully excited, as seen for  $0 < \eta \leq 0.045$  in Table 1. The critical buckling positions  $\sigma_{\text{cri}}$  given in the table are estimated by linearly fitting the lateral displacement of the midspan after the arch flops out-of-plane and extrapolating back to  $x(L/2) = 0$ , as demonstrated in Fig. 13(a) for the case  $\eta = 0.04$ .

The delay effect due to the speed of the point load is quantified by the log–log plot given in Fig. 13(b), where the estimated delay  $\Delta\sigma_{\text{cri}}$  of the critical buckling position is plotted against the dimensionless speed  $\eta$ . The data points are seen to fall neatly on a straight line, suggesting power-law dependence. A least-squares fit gives

$$\log \Delta\sigma_{\text{cri}} = \log 46.016 + 1.6774 \log \eta. \quad (5.3)$$

We therefore predict the delay to have superlinear dependence on the speed  $\eta$  with exponent 1.6774.

X. Zhao & G. H. M. van der Heijden

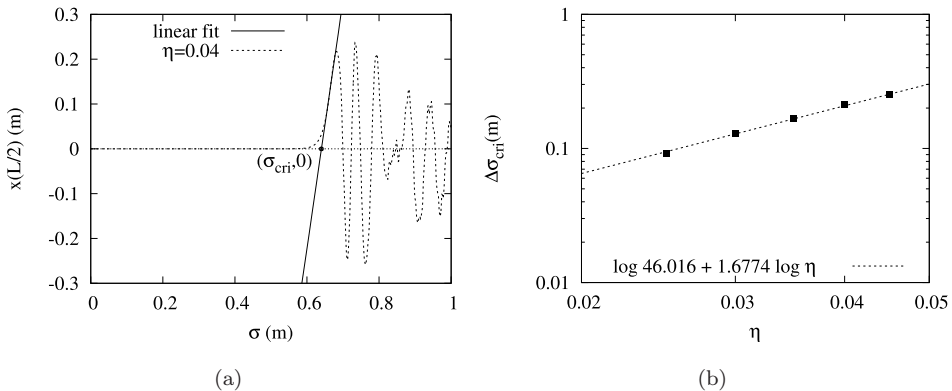


Fig. 13. (a) Linear extrapolation to determine the position  $\sigma = \sigma_{cri}$  of the load at buckling for the case where  $\eta = 0.04$ . (b) Log–log plot of the delay in the critical load positions at varying load speeds.

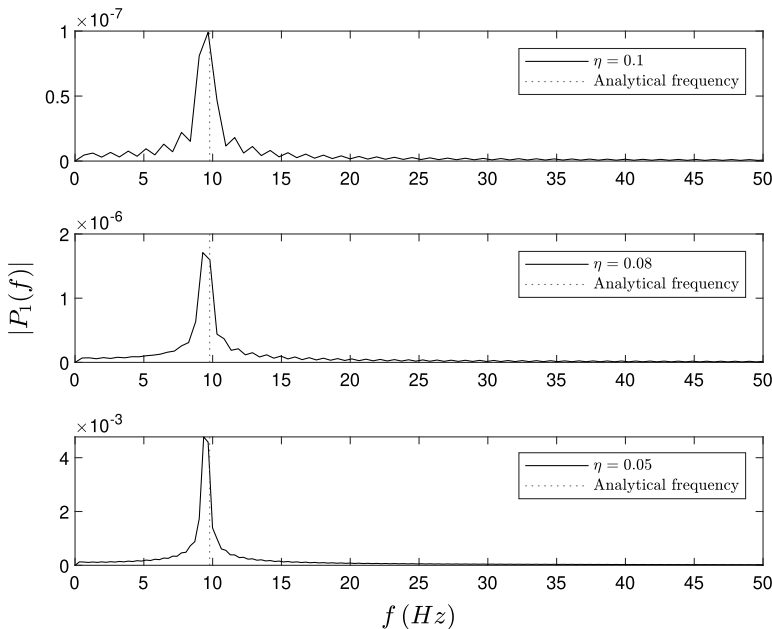


Fig. 14. Single-sided spectra for free out-of-plane oscillation of the arch midspan position  $x(L/2)$ , with frequency  $f$ , after the point load has left the arch, for different traveling speeds.

After the point load has left the arch at  $\sigma = L$  the arch performs free vibrations. To verify that the frequency of free out-of-plane vibrations agrees with the natural frequency of small arch vibrations calculated in Appendix B, we carry out a spectral analysis. Power spectrum plots for out-of-plane midspan oscillations in Fig. 14

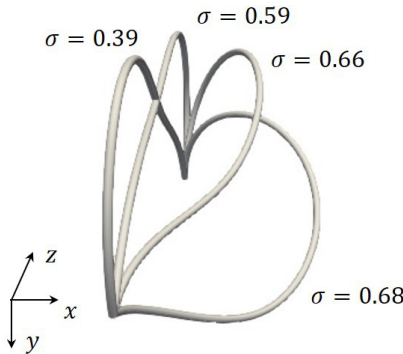


Fig. 15. True-view shapes of the arch under a point load traveling at speed  $\eta = 0.045$  with arclength positions of the load given.

show sharply-peaked frequency distributions with dominant frequency 9.671234 for  $\eta = 0.1$ , giving a 1% error compared to the analytical out-of-plane frequency  $\omega_1/(2\pi) = 9.784787$ , where  $\omega_1$  is taken from (B.3). The error gets larger for smaller  $\eta$  as larger deformations of the arch are triggered by a more slowly traveling load, pushing the deformations outside linear theory. For  $\eta = 0.08$ , the dominant frequency is 9.284384 (5% error). For  $\eta = 0.05$ , the dominant frequency is 9.349106 (4% error).

Figure 15 shows 3D deformations of the arch at various arclength positions of a load traveling at a speed of  $\eta = 0.045$ .

## 6. Conclusion

We have studied instability of a flexible circular arch under the action of a point load traversing at constant speed. Our focus has been on situations in which in the quasi-static (zero-speed) limit the arch suffers sideways flopping. For this we had to select a relatively large opening angle for the arch ( $\alpha = 160^\circ$ ) and a point load of intermediate magnitude ( $FL^2/EI = 36$ ). For other arch/load combinations failure, if it occurs, is dominated by in-plane collapse.

Having identified a case of out-of-plane instability we then performed a dynamical analysis, with full account of inertial effects, to investigate the onset of 3D bending-torsional deformation and vibration. We find that speed has a significant effect on arch stability. Significant out-of-plane displacements, where quasi-static analysis would predict them, can be avoided by relatively large traveling speeds ( $\eta \gtrsim 0.1$  for the parameters chosen in this paper). At relatively low speeds ( $\eta \lesssim 0.045$ ), out-of-plane deformations are fully excited and the arch oscillates about either the unstable planar static equilibrium or the stable out-of-plane static equilibrium.

We have quantified the delay effect of speed on the onset of buckling by a numerical power law also reported in recent studies of dynamically induced buckling.<sup>31,32</sup> In a future publication we hope to report on supporting analytical work for the observed delay effect of the speed of a moving load on arch buckling. Power-law dependence often signals universal behavior. It would be interesting to explore whether the critical exponent found here would extend to arches of different, non-circular, shape, or, if not, how the exponent varies.

### Acknowledgments

The support from the National Natural Science Foundation of China (Grant No. 52106263) and Project of Nurturing Doctoral Degree Awarding Authority for Mechanics, USST (Grant No. XWDA2021104) are gratefully acknowledged.

### Appendix A. Natural Frequencies of In-Plane Vibrations of a Hinged Circular Arch

We use the Rayleigh–Ritz approach of Ref. 33 to find the fundamental frequency of small (anti-symmetric) in-plane arch vibrations.

Let  $u, v, w$  be small displacements in the out-of-plane ( $x$ ), radial and tangential directions, respectively. Within linear small-deformation theory the in-plane bending moment is given by

$$M_x = EI_x \left( \frac{\partial^2 v}{\partial s^2} + \frac{1}{R} \frac{\partial w}{\partial s} \right) = EI_x \left( \frac{\partial^2 v}{\partial s^2} + \frac{v}{R^2} \right),$$

where we have used the inextensibility constraint  $\partial w / \partial s = v/R$ .

The boundary conditions are (for all  $t$ )

$$v = w = M_x = 0 \quad \text{at} \quad s = 0 \quad \text{and} \quad s = L.$$

The potential and kinetic energies for in-plane vibrations,  $U_i$  and  $T_i$ , are given by

$$U_i = \frac{1}{2} \int_0^L \frac{M_x^2}{EI_x} ds, \quad T_i = \frac{1}{2} \rho A \int_0^L \left( \left( \frac{\partial v}{\partial t} \right)^2 + \left( \frac{\partial w}{\partial t} \right)^2 \right) ds.$$

We write for the small vibrations  $u(s, t) = \bar{u}(s) \sin \omega t$ , etc. and define the Rayleigh–Ritz “action”  $Q$  as

$$Q = U_{i,\max} - \omega^2 T_{i,\max},$$

where

$$U_{i,\max} = \frac{1}{2} EI_x \int_0^L \left( \frac{d^2 \bar{v}}{ds^2} + \frac{\bar{v}}{R^2} \right)^2 ds, \quad T_{i,\max} = \frac{1}{2} \rho A \int_0^L (\bar{v}^2 + \bar{w}^2) ds.$$

We allow for arbitrary anti-symmetric radial mode shapes and take the expansion

$$\bar{v}(s) = \sum_{n=2,4,\dots}^{\infty} a_n \sin \frac{n\pi s}{L},$$

which satisfies the  $v$  and  $M_x$  boundary conditions. We impose the boundary condition for  $\bar{w}(s) = \frac{1}{R} \int_0^s \bar{v} \, ds$  at  $s = L$  by means of a Lagrange multiplier.

Thus, extremizing  $Q$  subject to this boundary condition constraint gives a system of linear equations for the coefficients  $a_n$  whose determinant condition for a nontrivial solution yields the frequency equation

$$\sum_{n=2,4,\dots}^{\infty} \frac{(\alpha/\pi)^2 \delta}{n^2[(\alpha/\pi)^2 - n^2]^2 - \delta[n^2 + (\alpha/\pi)^2]} = \frac{1}{2}, \quad (\text{A.1})$$

where  $\alpha = L/R$  is the arch's opening angle and  $\delta$  is introduced as dimensionless frequency squared,  $\omega^2$ . The solutions  $\delta_1, \delta_2, \dots$  of this equation give the natural frequencies as

$$\omega_i = \sqrt{\delta_i} \pi^2 \sqrt{\frac{EI}{\rho AL^4}} \quad (i = 1, 2, \dots),$$

where  $I = I_x$ .

The series in (A.1) converges very rapidly. Taking only the first term gives for the approximate fundamental frequency

$$\delta_1 = \frac{4[(\alpha/\pi)^2 - 4]^2}{4 + 3(\alpha/\pi)^2}, \quad (\text{A.2})$$

corresponding to a mode with anti-symmetric radial and symmetric axial displacements (with respect to the midpoint of the arch). Note that in the straight limit ( $\alpha = 0$ ) this result corresponds to the lowest anti-symmetric mode (i.e. having a node in the middle) of a hinged beam ( $\delta_1 = 16$ ). The result also makes sense in the case  $\alpha = 2\pi$ : for this angle the ends of the arch coincide and there is a rigid-body mode of rotation about the end hinges, causing a zero frequency.

For our case of  $\alpha = 160^\circ = \frac{8}{9}\pi$  and our standard parameters given in Sec. 4, (A.2) yields for the fundamental frequency

$$\omega_1 = 81.0215 \text{ s}^{-1} \quad (\delta_1 = 67\,600/10\,449 = 6.46952). \quad (\text{A.3})$$

The exact value (computed by taking more terms in the series) is

$$\omega_1 = 80.9899 \text{ s}^{-1} \quad (\delta_1 = 6.46448).$$

For this value of  $\alpha$ , symmetric radial modes have substantially higher natural frequencies.<sup>33</sup>

## Appendix B. Natural Frequencies of Out-of-Plane Vibrations of a Hinged Circular Arch

Here, we follow the approach in Ref. 34 but extend the discussion with some analytical results.

Using the same notation  $u, v, w$  as in Appendix A and  $\beta$  for the angular displacement of the cross-section of the arch due to torsion, the out-of-plane bending and twisting moments can be written as

$$M_y = EI_y \left( \frac{\beta}{R} - \frac{\partial^2 u}{\partial s^2} \right), \quad M_z = GJ \left( \frac{\partial \beta}{\partial s} + \frac{1}{R} \frac{\partial u}{\partial s} \right).$$

The boundary conditions are (for all  $t$ )

$$u = \frac{\partial u}{\partial s} = \beta = 0 \quad \text{at} \quad s = 0 \quad \text{and} \quad s = L.$$

The potential and kinetic energies for out-of-plane vibrations,  $U_o$  and  $T_o$ , are given by

$$U_o = \frac{1}{2} \int_0^L \left( \frac{M_y^2}{EI_y} + \frac{M_z^2}{GJ} \right) ds, \quad T_o = \frac{1}{2} \rho A \int_0^L \left( \frac{\partial u}{\partial t} \right)^2 ds,$$

where we have ignored rotational inertia (negligible for our slender arch for which the dimensionless ratio of rotational to translational inertia is  $I/(AL^2) = \frac{1}{4}(r/L)^2 = 6.25 \times 10^{-6}$ ).

We again define the Rayleigh–Ritz “action”  $Q$  as

$$Q = U_{o,\max} - \omega^2 T_{o,\max},$$

where

$$U_{o,\max} = \frac{1}{2} EI_y \int_0^L \left( \frac{\bar{\beta}}{R} - \frac{d^2 \bar{u}}{ds^2} \right)^2 ds + \frac{1}{2} GJ \int_0^L \left( \frac{d\bar{\beta}}{ds} + \frac{1}{R} \frac{d\bar{u}}{ds} \right)^2 ds,$$

$$T_{o,\max} = \frac{1}{2} \rho A \int_0^L \bar{u}^2 ds.$$

Confining ourselves to symmetric mode shapes, we now choose the expansions

$$\bar{u} = \sum_{n=0,2,4,\dots}^{\infty} a_n \cos \frac{n\pi s}{L}, \quad \bar{\beta} = \sum_{n=0,2,4,\dots}^{\infty} b_n \cos \frac{n\pi s}{L}, \quad (\text{B.1})$$

which satisfy the  $\frac{\partial u}{\partial s}$  boundary conditions, and impose the  $u$  and  $\beta$  boundary conditions by means of Lagrange multipliers.

Thus, extremizing  $Q$  subject to these boundary condition constraints gives a system of linear equations for the coefficients  $a_n, b_n$  whose determinant condition

for a nontrivial solution can be written as  $|D| = 0$  with  $D = D_1 + D_2$ , where

$$D_1 = \begin{pmatrix} A_2 & B_2 & 0 & 0 & \dots \\ B_2 & C_2 & 0 & 0 & \\ 0 & 0 & A_4 & B_4 & \\ 0 & 0 & B_4 & C_4 & \\ \dots & & & & \dots \end{pmatrix}, \quad D_2 = \begin{pmatrix} 2A_0 & 0 & 2A_0 & 0 & \dots \\ 0 & 2C_0 & 0 & 2C_0 & \\ 2A_0 & 0 & 2A_0 & 0 & \\ 0 & 2C_0 & 0 & 2C_0 & \\ \dots & & & & \dots \end{pmatrix},$$

and

$$\begin{aligned} A_n &= \frac{1}{2}EI_yL\left(\frac{n\pi}{L}\right)^4 + \frac{1}{2}GJ\frac{L}{R^2}\left(\frac{n\pi}{L}\right)^2 - \frac{1}{2}\omega^2\rho AL, \\ B_n &= \frac{1}{2}(EI_y + GJ)\frac{L}{R}\left(\frac{n\pi}{L}\right)^2, \\ C_n &= \frac{1}{2}EI_y\frac{L}{R^2} + \frac{1}{2}GJL\left(\frac{n\pi}{L}\right)^2. \end{aligned}$$

Taking the first two terms in the expansions (B.1) gives for this determinant condition

$$\begin{vmatrix} A_2 + 2A_0 & B_2 \\ B_2 & C_2 + 2C_0 \end{vmatrix} = 0.$$

Writing the natural frequencies as

$$\omega_i = \mu_i \sqrt{\frac{EI}{\rho AL^4}} \quad (i = 1, 2, \dots),$$

where  $I = I_y$ , this gives for the coefficient for the fundamental frequency  $\mu_1$  the approximate expression

$$\mu_1^2 = \frac{4\pi^2(16\pi^4 + 3\alpha^4 + 8\pi^2\alpha^2\nu)}{3[4\pi^2 + 3(1 + \nu)\alpha^2]}. \quad (\text{B.2})$$

Here  $\alpha = L/R$  and  $\nu = \frac{EI}{GJ} - 1$ ,  $J = 2I$ , is Poisson's ratio. The corresponding fundamental mode has symmetric out-of-plane displacement and twist angle (with respect to the midpoint of the arch).

In the straight limit,  $\alpha = 0$ , (B.2) gives an approximation for the fundamental frequency of a clamped beam:  $\mu_1 = 4\pi^2/\sqrt{3} = 22.7929$ , while the exact result is  $4.73004^2 = 22.3733$ , giving an indication of the error made by taking only the first oscillatory term in the series (including the second one gives 22.4721).

For our case of  $\alpha = 160^\circ = \frac{8}{9}\pi$  and our standard parameters given in Sec. 4, (B.2) yields for the fundamental frequency

$$\omega_1 = 61.4796 \text{ s}^{-1} \quad (\mu_1 = 19.0488). \quad (\text{B.3})$$

The exact value (computed by taking more terms in the series (B.1) and correspondingly larger determinant) is

$$\omega_1 = 59.76 \text{ s}^{-1} \quad (\mu_1 = 18.51).$$

For this value of  $\alpha$ , anti-symmetric out-of-plane modes have substantially higher natural frequencies.<sup>34</sup>

## ORCID

Xingwei Zhao <https://orcid.org/0009-0004-3574-826X>

G. H. M. van der Heijden <https://orcid.org/0000-0002-0720-5469>

## References

1. L. Frýba, *Vibration of Solids and Structures under Moving Loads* (Springer Netherlands, Dordrecht, 1972), doi:10.1007/978-94-011-9685-7.
2. A. V. Pesterev, B. Yang, L. A. Bergman and C. A. Tan, Revisiting the moving force problem, *J. Sound Vib.* **261** (2003) 75–91, doi:10.1016/S0022-460X(02)00942-2.
3. H. Ouyang, Moving-load dynamic problems: A tutorial (with a brief overview), *Mech. Syst. Signal Process.* **25** (2011) 2039–2060, doi:10.1016/j.ymssp.2010.12.010.
4. Y. B. Yang, J. D. Yau, S. Urushdaze and T. Y. Lee, Historical review on resonance and cancellation of simply supported beams subjected to moving train loads: From theory to practice, *Int. J. Struct. Stab. Dyn.* **23** (2023) 2340008, doi:10.1142/S0219455423400084.
5. S. Mhatre, E. Boatti, D. Melancon, A. Zareei, M. Dupont, M. Bechthold and K. Bertoldi, Deployable structures based on buckling of curved beams upon a rotational input, *Adv. Funct. Mater.* **31** (2021) 2101144, doi:10.1002/adfm.202170261.
6. Y. Li, H. Yu, K. Yu, X. Guo and X. Wang, Reconfigurable three-dimensional mesostructures of spatially programmed liquid crystal elastomers and their ferromagnetic composites, *Adv. Funct. Mater.* **31** (2021) 2100338, doi:10.1002/adfm.202100338.
7. N. Hu and R. Burgueño, Buckling-induced smart applications: Recent advances and trends, *Smart Mater. Struct.* **24** (2015) 063001.
8. S. P. Timoshenko and J. M. Gere, *Theory of Elastic Stability*, 2nd edn. (McGraw Hill International, Singapore, 1985).
9. J. G. A. Croll and A. C. Walker, *Elements of Structural Stability* (Macmillan, London, 1972).
10. R. D. Ziemian, *Guide to Stability Design Criteria for Metal Structures*, 6th edn. (John Wiley & Sons, Hoboken, NJ, 2010).
11. Y. J. Kang and C. H. Yoo, Thin-walled curved beams. II: Analytical solutions for buckling of arches, *ASCE J. Eng. Mech.* **120** (1994) 2102–2125.
12. R. C. Spoorenberg, H. H. Snijder, J. C. D. Hoenderkamp and D. Beg, Design rules for out-of-plane stability of roller bent steel arches with FEM, *J. Constr. Steel Res.* **79** (2012) 9–21, doi:10.1016/j.jcsr.2012.07.027.

13. D. B. La Poutré, R. C. Spoorenberg, H. H. Snijder and J. C. D. Hoenderkamp, Out-of-plane stability of roller bent steel arches — An experimental investigation, *J. Constr. Steel Res.* **81** (2013) 20–34, doi:10.1016/j.jcsr.2012.11.004.
14. M. A. Bradford, B. Uy and Y.-L. Pi, In-plane elastic stability of arches under a central concentrated load, *J. Eng. Mech.* **128** (2002) 710–719, doi:10.1061/(ASCE)0733-9399(2002)128:7(710).
15. Y.-L. Pi and M. A. Bradford, Nonlinear dynamic buckling of pinned-fixed shallow arches under a sudden central concentrated load, *Nonlinear Dyn.* **73** (2013) 1289–1306, doi:10.1007/s11071-013-0863-2.
16. J. S. Chen and J. S. Lin, Dynamic snap-through of a shallow arch under a moving point load, *J. Vib. Acoust.* **126** (2004) 514–519, doi:10.1115/1.1804991.
17. X. W. Zhao and G. H. M. van der Heijden, Planar dynamics of large-deformation rods under moving loads, *J. Sound Vib.* **412** (2018) 309–325, doi:10.1016/j.jsv.2017.09.037.
18. M. A. Bradford and Y.-L. Pi, A new analytical solution for lateral-torsional buckling of arches under axial uniform compression, *Eng. Struct.* **41** (2012) 14–23, doi:10.1016/j.engstruct.2012.03.022.
19. T. Usami and S. Y. Koh, Large displacement theory of thin-walled curved members and its application to lateral-torsional buckling analysis of circular arches, *Int. J. Solids Struct.* **16** (1980) 71–95.
20. X. W. Zhao, G. H. M. van der Heijden and Z. D. Hu, Vibrations of beams and rods carrying a moving mass, *J. Phys.: Conf. Ser.* **721** (2016) 012016, doi:10.1088/1742-6596/721/1/012016.
21. S. S. Antman, *Nonlinear Problems of Elasticity*, 2nd edn. (Springer, New York, 2005).
22. D. H. Hodges, Non-linear inplane deformation and buckling of rings and high arches, *Int. J. Non-Linear Mech.* **34** (1999) 723–737.
23. Y.-L. Pi, M. A. Bradford and B. Uy, In-plane stability of arches, *Int. J. Solids Struct.* **39** (2002) 105–125, doi:10.1016/S0020-7683(01)00209-8.
24. S. Goyal, N. C. Perkins and C. L. Lee, Nonlinear dynamics and loop formation in Kirchhoff rods with implications to the mechanics of DNA and cables, *J. Comput. Phys.* **209** (2005) 371–389, doi:10.1016/j.jcp.2005.03.027.
25. R. M. Murray, Z. Li and S. S. Sastry, *A Mathematical Introduction to Robotic Manipulation* (CRC Press, Boca Raton, FL, 2017), doi:10.1201/9781315136370.
26. J. Chung and G. M. Hulbert, A time integration algorithm for structural dynamics with improved numerical dissipation: The generalized- $\alpha$  method, *J. Appl. Mech.* **60** (1993) 371–375, doi:10.1115/1.2900803.
27. S. Erlicher, L. Bonaventura and O. S. Bursi, The analysis of the Generalized- $\alpha$  method for non-linear dynamic problems, *Comput. Mech.* **28** (2002) 83–104, doi:10.1007/s00466-001-0273-z.
28. U. Nowak and L. Weimann, A family of Newton codes for systems of highly nonlinear equations, Technical Report TR-91-10, Konrad-Zuse-Zentrum für Informationstechnik, Berlin (1991), <http://www.zib.de/weimann/NewtonLib/index.html>.
29. S. A. Eftekhari, A note on mathematical treatment of the Dirac-delta function in the differential quadrature bending and forced vibration analysis of beams and rectangular plates subjected to concentrated loads, *Appl. Math. Model.* **39** (2015) 6223–6242, doi:10.1016/j.apm.2015.01.063.
30. E. J. Doedel, A. R. Champneys, T. R. Fairgrieve, Y. A. Kuznetsov, B. Sandstede and X. J. Wang, AUTO97: Continuation and bifurcation software for ordinary differential equations (1997), <http://indy.cs.concordia.ca/auto>.

31. X. W. Zhao and G. H. M. van der Heijden, Dynamic torsional buckling: Prebuckling waves and delayed instability, *Commun. Nonlinear Sci. Numer. Simul.* **69** (2019) 360–369, doi:10.1016/j.cnsns.2018.09.017.
32. M. Liu, M. Gomez and D. Vella, Delayed bifurcation in elastic snap-through instabilities, *J. Mech. Phys. Solids* **151** (2021) 104386, doi:10.1016/j.jmps.2021.104386.
33. F. C. Nelson, In-plane vibrations of a simply supported circular ring segment, *Int. J. Mech. Sci.* **4** (1962) 517–527.
34. F. C. Nelson, Out-of-plane vibration of a clamped circular ring segment, *J. Acoust. Soc. Am.* **35** (1963) 933–934.